Numerical Simulation of a Tornado Vortex

LEWIS D. GRASSO AND WILLIAM R. COTTON

Department of Atmospheric Science, Colorado State University, Fort Collins, Colorado

(Manuscript received 29 October 1993, in final form 19 September 1994)

ABSTRACT

A two-way interactive, nested-grid simulation of a rotating supercell thunderstorm was performed. After 90 min the genesis of a descending incipient tornado vortex initially located aloft was simulated. The associated pressure-deficit tube subsequently built downward into the subcloud layer, where it continually fed upon a low-level source of vertical vorticity possibly introduced by the low-level downdraft. The pressure-deficit tube then drew in the low-level vorticity-rich air, allowing it to descend to the surface. A strong vortex thus formed in the subcloud field.

1. Introduction

Nonhydrostatic numerical prediction cloud models have successfully simulated many of the gross features of supercell thunderstorms (Schlesinger 1978, 1980; Klemp and Wilhelmson 1978a,b; Wilhelmson and Klemp 1981; Tripoli and Cotton 1986; Weisman and Klemp 1982). Only limited attempts have been made to extend those simulations to investigation of the mechanisms of tornado formation. Instead, most of the effort at simulating tornado formation has been done with axisymmetric models (Lewellen 1976; Walko 1988) or axisymmetric laboratory vortex models (Ward 1972; Church et al. 1979; Snow 1982). It is, however, widely accepted that the parent cell of, and the inflow to, a tornado are highly three-dimensional (Davies-Jones 1984; Rotunno and Klemp 1985; Lilly 1986a,b).

From the perspective of axisymmetric numerical models or laboratory vortices, tornado genesis is achieved primarily from the concentration of ambient vorticity that is associated with the parent mesocyclone. There is evidence, however, that suggests that tornado formation in supercell thunderstorms is not in the center of the updraft but is instead in the zone of strong horizontal gradient of vertical velocity (Ray et al. 1976; Brandes 1978, 1984; Lemon and Doswell 1979).

In an attempt to enhance horizontal resolution in a simulated storm and retain the three-dimensional properties of a storm, Klemp and Rotunno (1983) performed a one-way nested simulation with a fine grid having 250-m horizontal grid spacing. This simulation revealed additional finestructure of the mesocyclone but still was not capable of resolving the tornado itself. Based on those results and additional simulations (Rotunno and Klemp 1985) they proposed that the primary source of low-level rotation responsible for low-level mesocyclone formation is baroclinic production of horizontal vorticity along the gust front at the interface between the forward-flanking downdraft and the low-level storm inflow air. This horizontally oriented, baroclinically produced vorticity is then tilted into the vertical where it becomes a strong source of low-level rotation.

In this paper we describe the results of a three-dimensional interactive (two way) nested grid simulation of the 1977 Del City, Oklahoma, tornadic supercell storm, which provides sufficient horizontal resolution to depict many of the features of the genesis and evolution of a strong vortex in the subcloud region. This simulation yields new insight into the tornadogenetic process.

2. Experimental design

The Regional Atmospheric Modelling Systems (RAMS) developed at Colorado State University (Schmidt and Cotton 1990; Cram et al. 1992a,b) was used to perform the simulations. RAMS is a general modeling system that was developed from the earlier cloud model described by Tripoli and Cotton (1980, 1982, 1989a,b). The following is a brief description of the configuration used in this study.

- The nonhydrostatic, time-split compressible version of RAMS was used. The wind components u, v, and w, ice/liquid water potential temperature, dry-air density, total water mixing ratio, and the mixing ratio of the various hydrometeor species, including ice, are predicted. From these variables, pressure, potential

Corresponding author address: Dr. Lewis D. Grasso, Dept. of Atmospheric Science, Colorado State University, Fort Collins, CO 80523.

temperature, temperature, water vapor mixing ratio, and cloud water mixing ratio are diagnosed.

- The cloud microphysics module (Cotton et al. 1982, 1986; Flatau et al. 1989) consists of a bulk microphysics scheme in which the mixing ratios of pristine ice crystals, aggregates, graupel, and raindrops are predicted assuming a characteristic diameter. The concentration of ice crystals is also predicted. Nucleation, vapor deposition, collection, and precipitation sedimentation are included. Hail was not simulated as a distinct species but is lumped into the graupel class.
- Vertical and horizontal turbulent mixing was parameterized using the Smagorinsky (1963) deformation scheme with the Lilly (1962) modifications for stability. The Louis (1979) surface-layer scheme was used with specified surface fluxes.
- The numerical procedures described by Tripoli and Cotton (1982, 1989a,b) consist of leapfrog time differencing with an Asselin filter, a second-order spatial advection on a standard Arakawa C grid (Arakawa and Lamb 1981).
- A two-way nesting procedure was used based on the scheme described by Clark and Farley (1984). This algorithm allows fine grids to communicate with coarse grids and vice versa.
- The coarse grid was set up with 1-km grid spacing in each horizontal direction and a stretched vertical grid with the lowest grid spacing equaling 25 m near the ground. The vertical stretching ratio is 1.2 until a vertical grid spacing of 666 m is obtained. The vertical grid spacing is then kept fixed at this value to the top of the grid domain. This choice of a stretched grid was selected to obtain high resolution from the surface to a few kilometers elevation to capture the formation of the tornado. The horizontal domain is 40 km × 40 km and the vertical domain is 16 km high. A forward time step of 5 s was chosen prior to spawning two finer grids.
- Radiative heating and Coriolis force was not included.
- The top boundary condition was a wall on top with seven Rayleigh friction absorption layers from the top. The lateral boundary condition is the Klemp–Wilhelmson (1978a,b) radiation condition. The lower boundary is rigid with turbulent fluxes of heat, moisture, and momentum provided by the Louis (1979) surface-layer parameterization (note that the lower boundary is not free slip).
- No soil or vegetation model is included. Any precipitation that falls on the lower boundary is removed so as to prevent any buildup.

The model was initialized horizontally homogeneously with a special sounding, shown in Fig. 1, from 20 May 1977, the day of the Del City tornadic storm (Ray et al. 1981). A rectangular warm bubble was released in the middle of the domain. The bubble center was 1.5 km high, and its horizontal and vertical dimensions were 10 km and 3 km, respectively. The temperature was 1.5 K warmer and the water vapor mixing ratio was 2 g kg^{-1} greater, uniformly in the bubble, than in the environment. These values were chosen to trigger convection in the model without leading to numerical instabilities for the time step chosen. The wind hodograph for this simulation is shown in Fig. 2. The simulation was run forward 90 min, at which time two finer grids were spawned.

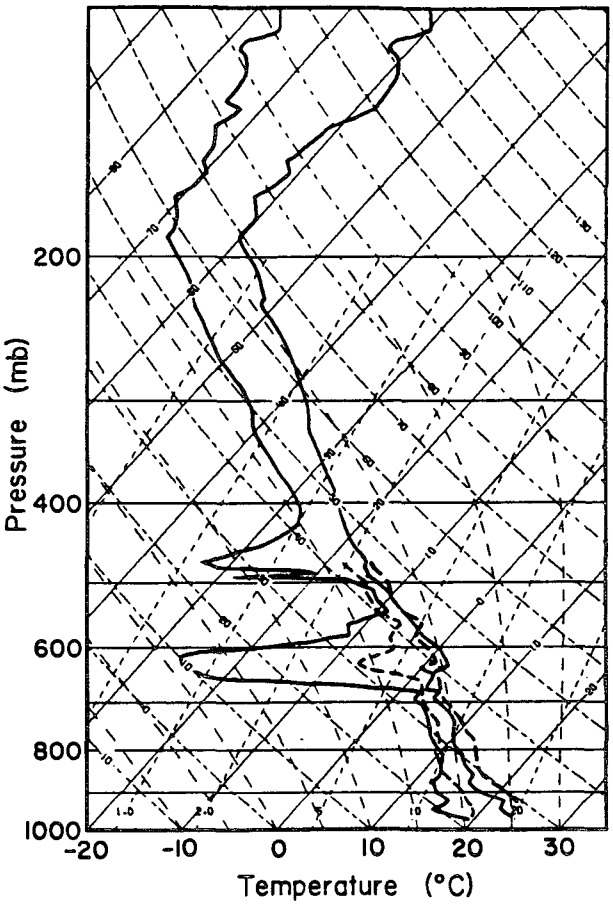

FIG. 1. Temperature and dewpoint soundings taken from Elmore City, Oklahoma, at 1620 (heavy solid line) and Fort Still, Oklahoma, at 1500 (heavy dashed lines) 20 May 1977 (from Klemp et al. 1981).

Grid 2 was 10 km × 10 km on a side with a horizontal grid spacing of 333 m. The third interactive grid was 4 km × 4 km horizontally with a grid spacing of 111 m. The vertical grid spacing in both fine grids was the same as the first grid.

The time step was reduced to prevent computational instabilities from growing due to the reduction in horizontal grid spacing. The large grid simulation was run with a new time step of one second, the intermediate one with a time step of one-third of a second, and the finest one with a time step of one-ninth of a second. The three-dimensional fields were stored every 60 s for future analysis for the next 17 simulated minutes. Each

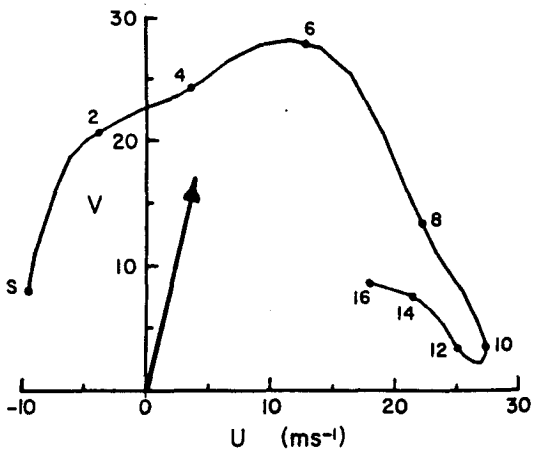

FIG. 2. Composite smoothed hodograph of environmental winds based on the 1500 Fort Still and 1620 Elmore City soundings. The heights (km) above sea level are labeled along the profile. The observed propagation speed of the Del City storm during its mature phase is indicated by the heavy arrow (from Klemp et al. 1981).

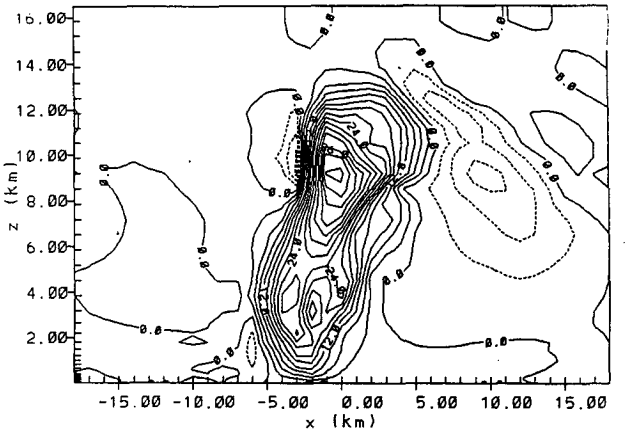

FIG. 3. Vertical cross section of vertical motion at y = −1.0 km and at 95 min into the simulation. The contour interval is 3.0 m s^{-1}. The solid contour is upward motion and the dashed is downward. The maximum upward is 45.0 m s^{-1} and the maximum downward is 9.0 m s^{-1}.

1-min run required 12 h of real time on a single processor of a Stardent 3040 RISC workstation.

3. Simulated mesocyclone structure

Following the introduction of an initial heat and moisture source, the simulation proceeded similar to earlier simulations of supercell thunderstorms in a wind profile with a clockwise-rotating hodograph (Klemp and Wilhelmson 1978a,b; Weisman and Klemp 1984). The initial cell split, and the right cell became dominant.

After 95 min, with the high-resolution simulation running for 5 min, an east–west vertical cut just to the north of the cloudbase updraft center shows a conspicuous updraft and downdraft feature (see Fig. 3). The main updraft extends to about 14 km above ground level. The maximum updraft for this cross section is at 9 km and is 45 m s^{-1}. The updraft also exhibits an eastward lean with height of some 5 km in the horizontal direction. The main downdraft in this figure may be a result of hydrometeors being ejected out of the top of the storm where the anvil canopy is forming. The strongest downdraft is at 9 km and is 9 m s^{-1}. A smaller downdraft can also be seen to the west of the main updraft at 10 km. The very small low-level downdraft to the west of the updraft just below 2 km is in response to the precipitation field.

The perturbation pressure field in the same vertical cross section, shown in Fig. 4, indicates that a very large percentage of the main updraft is characterized by low pressure. The largest pressure deficit is found at roughly a few hundred meters above cloud base with a magnitude of 5.2 mb. A high pressure region is located at 12 km and is associated with the overshooting top of the storm. One can see in Fig. 3 that the storm's updraft is experiencing rapid deceleration into the high pressure region.

The perturbation temperature field for the same vertical cross section, shown in Fig. 5, indicates that a warm column extends from 2 km above ground level to 12 km and is capped by a very large cold dome. The maximum temperature excess is 9 K, located just above 6 km or roughly the middle levels of the storm. It should be mentioned that using a skew T–log$p$ diagram to estimate the temperature excess available to the storm will provide an underestimate due to the fact that the moist adiabats do not take into account the heat release due to the ice deposition/freezing process. Entrainment can reduce the temperature excess, but in the nearly unmixed updraft cores, there is only small compensation for the neglect of the ice-phase heating.

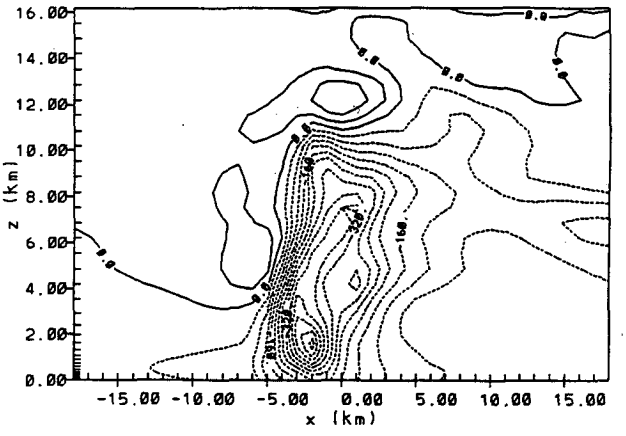

FIG. 4. Perturbation pressure field in the same vertical cross section as the previous figure. Contour interval is 40 Pa. The dashed contour is negative perturbation and the solid is positive perturbation.

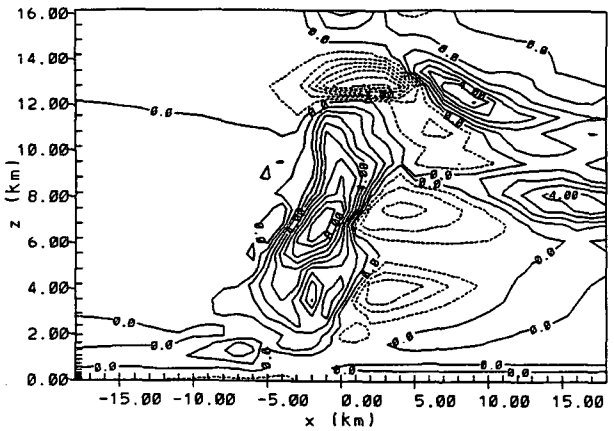

FIG. 5. Perturbation temperature field in the same vertical cross section as Fig. 3. The contour interval is 1°C. The solid lines depict positive perturbations and the dashed negative perturbations.

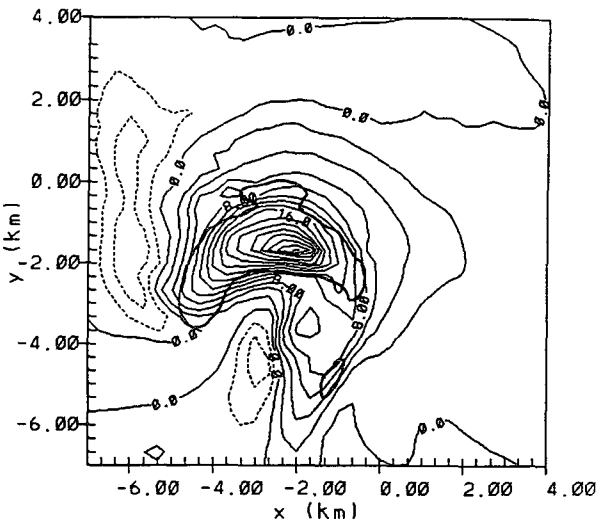

FIG. 7. Horizontal cross section of vertical motion at 1095 m and 95 min into the simulation. The contour interval is 2.0 m s^{-1}. The maximum upward motion is 30.0 m s^{-1} and the maximum downward is -4.0 m s^{-1}. The dark solid depicts the boundary, vertical vorticity of 0.01 s^{-1} for the mesocyclone.

Figure 6 shows the rain mixing ratio field. This field exhibits a distinct downshear tilt with height. The low-level maximum of 10 g kg^{-1} is just above the vault or weak echo region located between $x = -5.0$ km and $x = -1.0$ km and bounded above at $z = 3.0$ km. Located 10 km above ground is a secondary maximum of 6.0 g kg^{-1}. When compared to the vertical motion field one sees that the low-level downdraft located at $x = -6.0$ km and below 2.0 km is correlated nicely with the rain field in Fig. 6. The echo-free vault is also filled with updraft as would be expected.

The vertical motion field in Fig. 7 is a horizontal cross section at 1095 m AGL, approximately cloud base. The updraft is generally comma shaped with the maximum updraft speed of 30 m s^{-1} in the core. Two distinct downdrafts are seen. The one located to the west is associated with precipitation and has a magnitude of 4 m s^{-1}. A smaller downdraft directly to the south of the updraft is not associated with the precipitation field. The magnitude of this downdraft is also 4 m s^{-1}.

The horizontal, storm-relative wind components, shown in Fig. 8 for the same height as the last figure, show the inflow region to the east and southeast of the main updraft. The environmental air from the east and southeast converges and accelerates into the storm continually supplying warm moist air. Of particular interest is the deformation field located roughly at $x = -4.0$ and $y -4.0$ km. This field is just west of the small

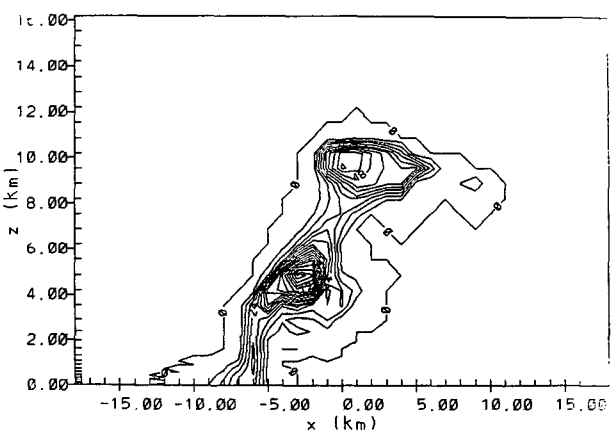

FIG. 6. Same as in Fig. 3 for the rain mixing ratio field. The contour interval is 0.6 g kg^{-1}. The maximum value is 10.2 g kg^{-1}.

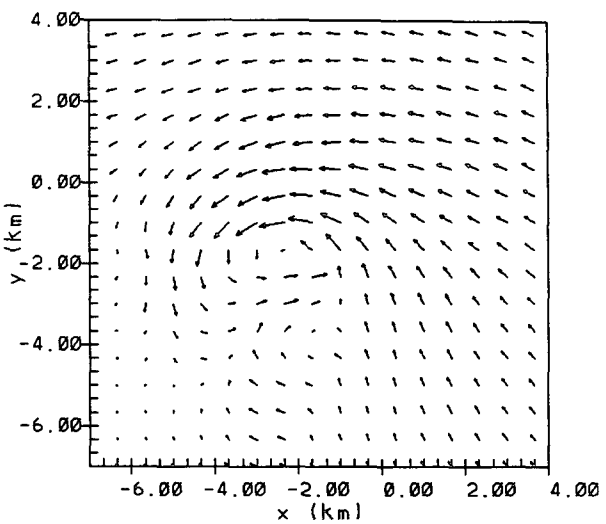

FIG. 8. Horizontal cross section of the horizontal storm-relative wind vectors at 1095 m and 95 min into the simulation. The maximum wind vector is 28.0 m s^{-1}.

downdraft located to the south of the main updraft and gives the updraft the appearance of a comma. This "clear slot" is a common feature in tornadic supercell thunderstorms (see Lemon and Doswell 1979; Ray 1986). If one were located directly underneath this region and looking at the updraft field directly to the east of this small downdraft, located on Fig. 7 from $y = -3.0$ to $y = -6.0$ km at $x = -2.0$ km, one would notice that the western side of the cumulus is sinking rapidly. The deformation pattern can be visually detected in real storms by looking at the cloud tags at cloud base to the northwest and to the southeast.

Figure 9 shows the rain mixing ratio at cloud base. The most conspicuous feature is the "hook" appearance. By comparing this field with the vertical motion field one sees that the updraft is devoid of rain. The southern hook appendage is northwest of the smaller downdraft and intrudes slightly into the updraft. The maximum liquid water content is located northwest and west of the updraft. The main downdraft is correlated well with this rain field. The region bordered by the rain field to the north, west, and south by the hook is the weak echo region and is an indication of a strong updraft.

Figure 10 shows the rain mixing ratio field at an altitude of 3528 m. Unlike the rain field at cloud base, the updrafts are completely filled with rain. Notice, however, at $x = -4.0$ km and $y -1.0$ km, that the smallest closed contour is a minimum in the local rain field. This minimum is bounded on all sides with heavier rain and is identified as the bounded weak echo region (BWER)—another signature of a potentially severe thunderstorm.

This simulation of the supercell has features that are consistent with other numerical results (Klemp and Rotunno 1983) and observations (Klemp et al. 1981; Brandes 1984); the main ones are as follows:

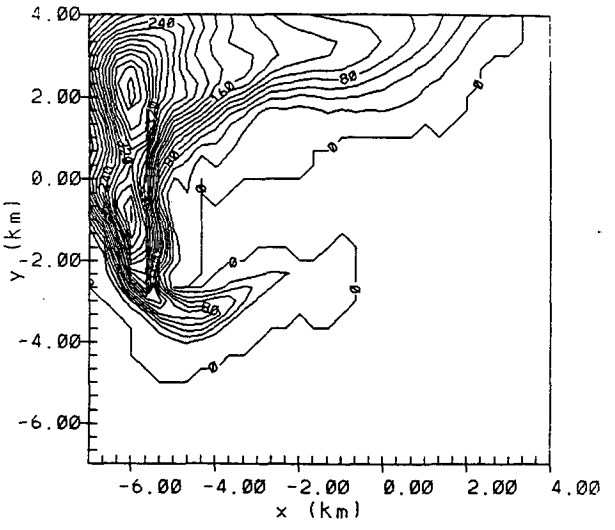

FIG. 9. Horizontal cross section as in Fig. 8 of rain mixing ratio depicting the hook echo. The contour interval is 0.2 g kg^{-1}. The maximum value is 4.2 g kg^{-1}.

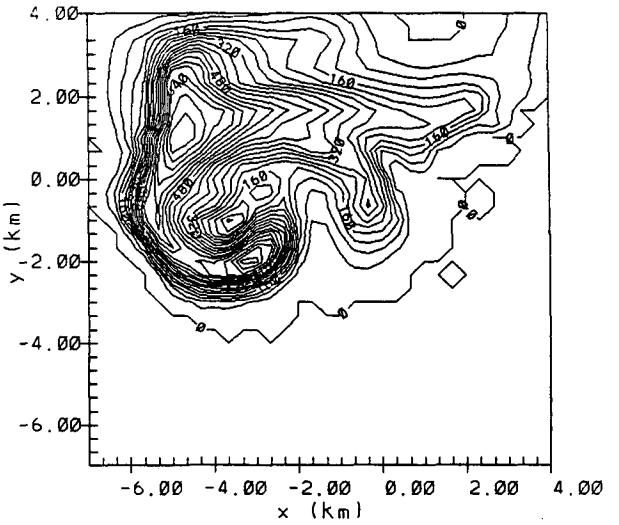

FIG. 10. Horizontal cross section of rain mixing ratio showing the bounded weak echo region at 3528 m and 95 min into the simulation. The contour interval is 0.4 g kg^{-1}. The maximum value is 7.6 g kg^{-1}.

1) storm motion of 15 m s^{-1} in this simulation and in Klemp et al. (1981) of 16 m s^{-1} to the north-northeast agrees well with the observed motion to the north-northeast of 17 m s^{-1};

2) updraft diameters of approximately 10 km;

3) cyclonically turning air trajectories in downdrafts;

4) updraft speeds of 30 m s^{-1} at midlevels;

5) hook signature at low levels;

6) horseshoe-shaped low-level updraft [in a later simulation Klemp and Rotunno (1983), with the aid of one-way nesting, were able to simulate this updraft feature];

7) two updraft centers at 3528 m [see Grasso (1992), his Fig. 3.17] consistent with the observed updraft field at 4 km [the Klemp et al. simulation was unable to reproduce this feature perhaps due to lack of resolution];

8) observed weak echo vault;

9) agreement between simulated storm relative winds on the coarse grids and observations;

10) storm top between 13 and 14 km.

4. Analysis of the pressure field and associated vortex

In section 3, we analyzed the mesocyclone structure as simulated on the first two grids. We now analyze the simulation of the downward propagation of the minimum in the pressure field and associated vortex on the finest grids. One feature that stood out well was the relationship between the updraft and the perturbation pressure fields.

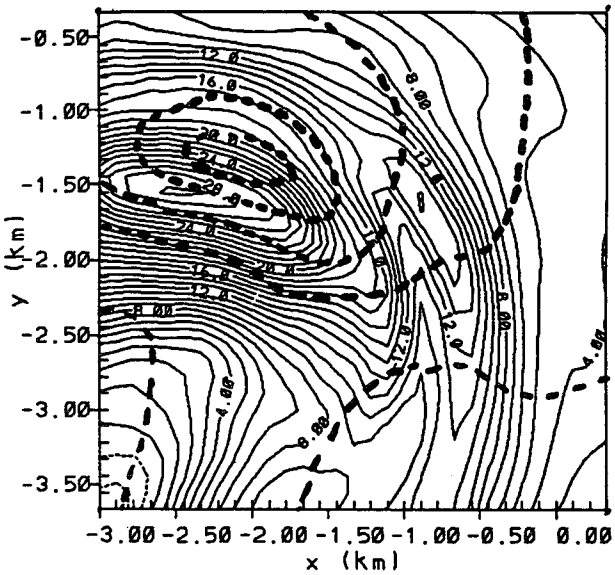

FIG. 11. Horizontal cross section at 1095 m and 94 min into the simulation. Solid contours depict upward motion contoured at 1 m s^{-1} and the bold dashed contours depict the perturbation pressure. The maximum updraft is 29 m s^{-1}. The contours for the pressure field are −120, −240, −360, −480, and −540 Pa.

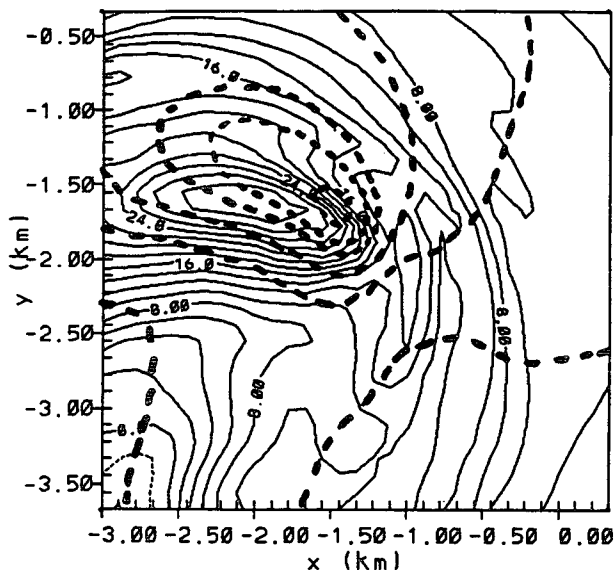

FIG. 12. Same as Fig. 11 at 95 min. The contours for the pressure field are −120, −240, −360, −480, −510, and −660 Pa.

Shown in Fig. 11 are the updraft (solid contours) and perturbation pressure (bold dashed contours) fields approximately at cloud base. The lowest pressure is collocated, to the north-northeast of the updraft core, with the horizontal gradient of upward motion. The maximum value of the perturbation pressure deficit is −540 Pa. One minute later (see Fig. 12), the pressure field has changed significantly. The lowest pressure has moved to the east of the updraft but is still in the gradient, in fact the largest horizontal gradient, of upward motion. The maximum value of the perturbation pressure deficit is −660 Pa, 120 Pa lower compared to one minute earlier.

The portion of the updraft located in the lower half, $y < -2.5$ km, of Figs. 11 and 12 is identified as the flanking line. The gust front at the surface is lifting air there. The small dashed contours in the lower left corner in both figures is the northern tip of the clear slot downdraft.

The vertical component of the vorticity field corresponding to Fig. 11 is shown in Fig. 13. The bulk of the updraft is characterized by cyclonic vorticity, as would be expected. Of particular interest is the overlap in the maximum value of positive vertical vorticity and the horizontal gradient of upward vertical motion at $x = -1.5$ km and $y = -1.75$ km.

At the same time as Fig. 11, Figs. 14 and 15 show the vertical vorticity fields at consecutively lower levels below cloud base. It is interesting to note that with decreasing height, the magnitude of the maximum positive vertical vorticity increases and its location shifts toward the southeast.

The vertical vorticity field at 95 min has changed significantly compared to one minute earlier (compare Figs. 16 and 13). The maximum value of positive vertical vorticity has increased and is clearly collocated with the largest horizontal gradient of upward vertical motion. Notice the change in the relationship between the pressure and vertical vorticity fields when comparing Figs. 11 and 13 to Figs. 12 and 16. In Fig. 12, the lowest pressure is located very close to the maximum positive vertical vorticity. It appears that the lowest

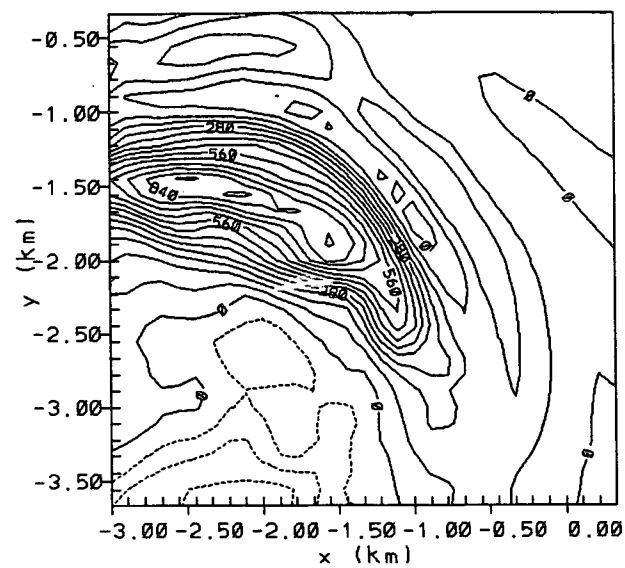

FIG. 13. Relative vertical vorticity at 1095 m and 94 min. Contour interval is 0.007 s^{-1}. The maximum is 0.091 s^{-1}.

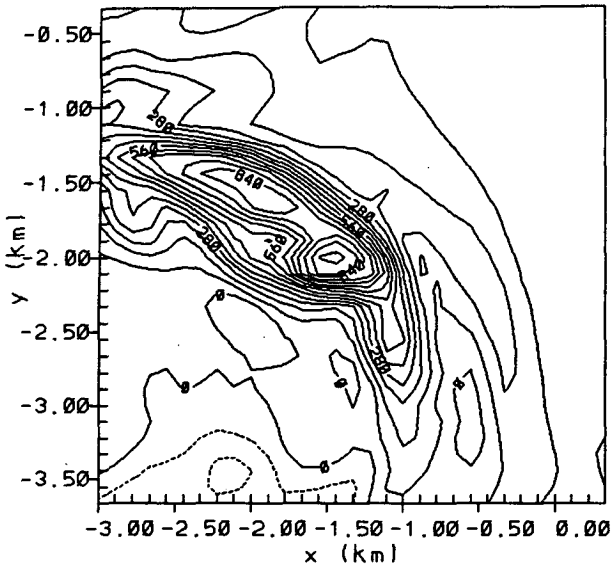

FIG. 14. Same as Fig. 13 at 722 m and 94 min. The maximum is 0.098 s^{-1}.

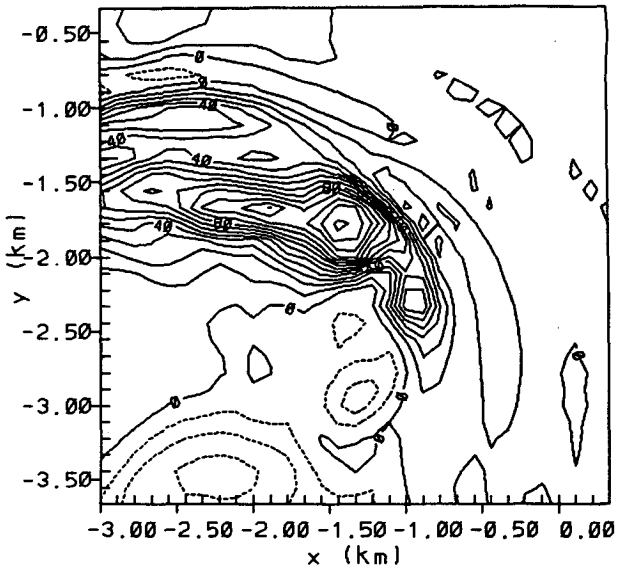

FIG. 16. Same as Fig. 13 at 1095 m and 95 min. The contour interval is 0.01 s^{-1} and the maximum is 0.13 s^{-1}.

pressure is moving toward, or is responding to, the local maximum of positive vertical vorticity in Fig. 16. Why should this be? Following Brandes (1984) we calculated the two dominant terms in the diagnostic equation for pressure, which to a good approximation are (see Grasso 1992)

$$\frac{\partial}{\partial x_i}\frac{\partial p^*}{\partial x_i} \approx -\rho_0(z) d_{ij} d_{ij} + \frac{\rho_0(z)}{2}\omega_j\omega_j, \qquad (1)$$

where the terms on the right-hand side are the rate-of-strain and vorticity forcing, respectively.

The result for calculations done at cloud base, shown in Fig. 17, indicate the dominant forcing is the total three-dimensional vorticity. Our results are consistent with those of Brandes (1984) for the same storm. Vorticity forcing was consistently dominant, by a factor of 3, over the rate-of-strain forcing at different model lev-

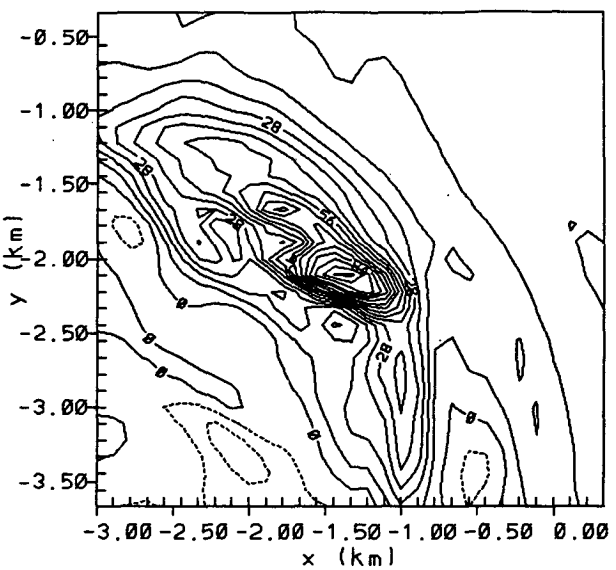

FIG. 15. Same as Fig. 13 at 463 m and 94 min. The maximum is 0.105 s^{-1}.

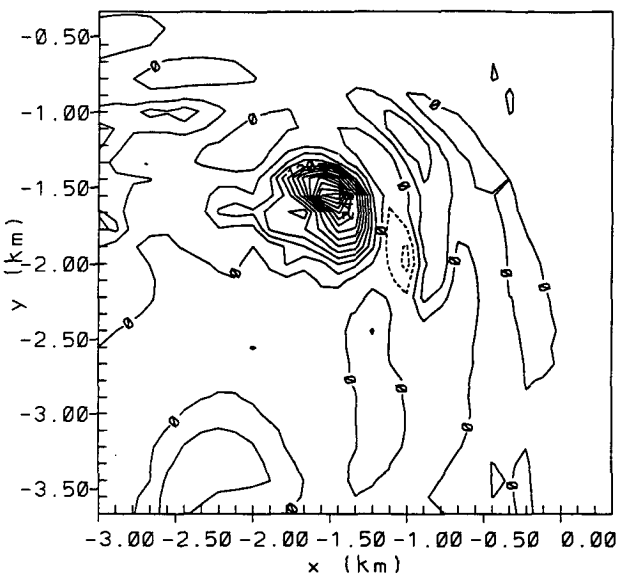

FIG. 17. Horizontal cross section at 1095 m at 96 min of vorticity divided by rate-of-strain forcing. Solid (dashed) contours indicate where the vorticity forcing is larger (smaller) than the strain forcing. The contour interval is 30 and the maximum is 390.

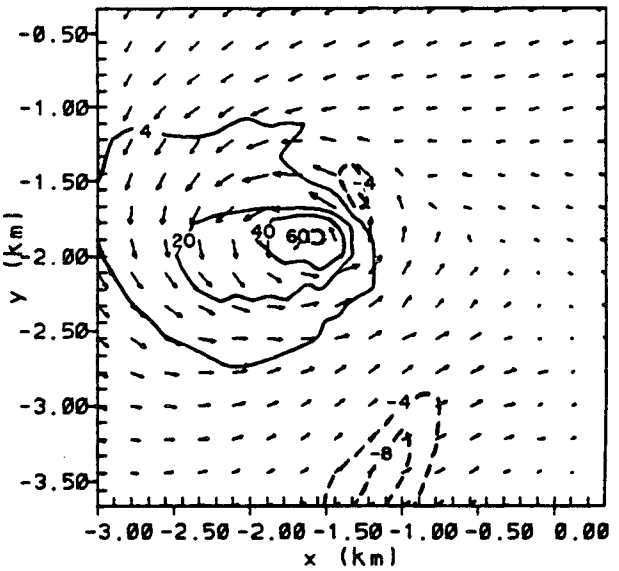

FIG. 18. Horizontal cross section at 365 m and 105 min of the storm-relative horizontal wind vectors superimposed on the vertical motion field. The largest vector is 54 m s^{-1}. The updraft contours (solid) are 4, 20, 40, and the maximum of 60 m s^{-1}. The downdraft to the northeast of the updraft is -4 m s^{-1} and to the south is -4 and -8 m s^{-1}.

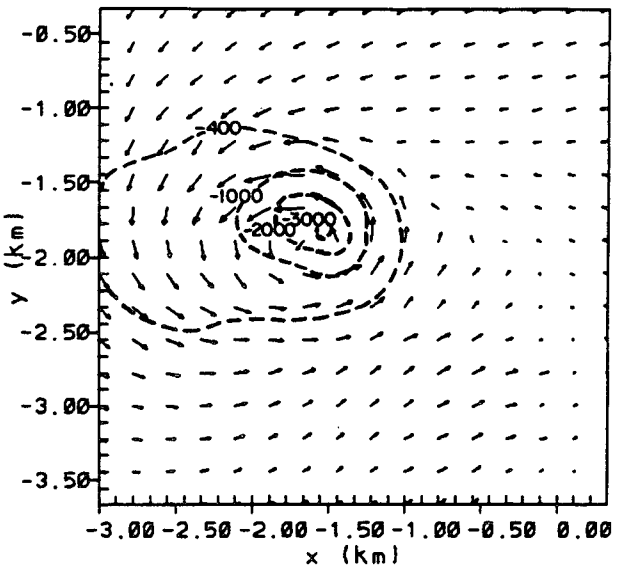

FIG. 19. Same as Fig. 18; the dashed contours are the perturbation pressure. Contours are -400, -1000, -2000, and the largest deficit -3000 Pa.

els and times. We do not anticipate the buoyancy forcing to have the same magnitude as the vorticity forcing near cloud base, and thus the term was neglected in the calculations.

The movement of the lowest pressure from its location in Fig. 11 to that in Fig. 12 seems to be in response to the total vorticity. That is, the increase of the positive vertical vorticity in the horizontal gradient of upward motion east of the updraft core may have drawn the pressure minimum toward the southeast away from its original location and deepened it somewhat.

The vertical vorticity field has vertical continuity in the lowest 1 km. It appears to us that the vertical advection and horizontal convergence of this vorticity is what causes the positive vertical vorticity maximum to form and to be maintained to the east-southeast of the updraft core near cloud base (see Figs. 13 and 16).

At the surface at 95 min, the lowest pressure is still to the north of the updraft core, while at cloud base it is to the east-southeast. In the vertical is a high–low pressure couplet from the surface to cloud base along the east-southeast side to the updraft. This pressure pattern is reminiscent of the high–low pressure couplet, in the vertical, due to the clockwise turning of the shear vector with height across the updraft of the supercell thunderstorm. The rightward turning of the storm is due to the enhanced upward acceleration along the right side of the storm due to the couplet. Similarly, the pressure pattern in our case will enhance the upward acceleration of parcels toward the pressure minimum at cloud base. In response to this, horizontal convergence can enhance vertical vorticity beneath the pressure minimum. As a result, the flow takes on a more rotational characteristic, and the pressure will fall beneath the pressure minimum at cloud base. The descent of the incipient tornado vortex thus begins.

The set of Figs. 18 to 27 shows the updraft, pressure, and storm-relative horizontal velocity vector fields at the mature stage of the vortex. The most intense part

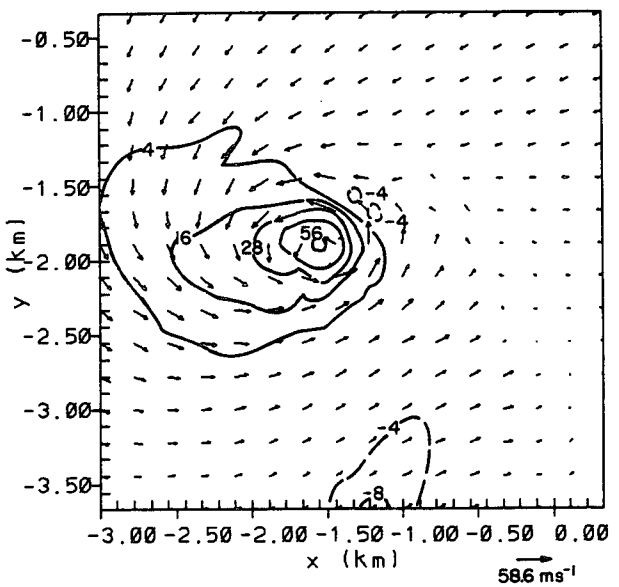

FIG. 20. Horizontal cross section at 283 m and 105 min. Solid (dashed) contours depict upward (downward) motion in meters per second. The storm-relative horizontal wind is shown as arrows.

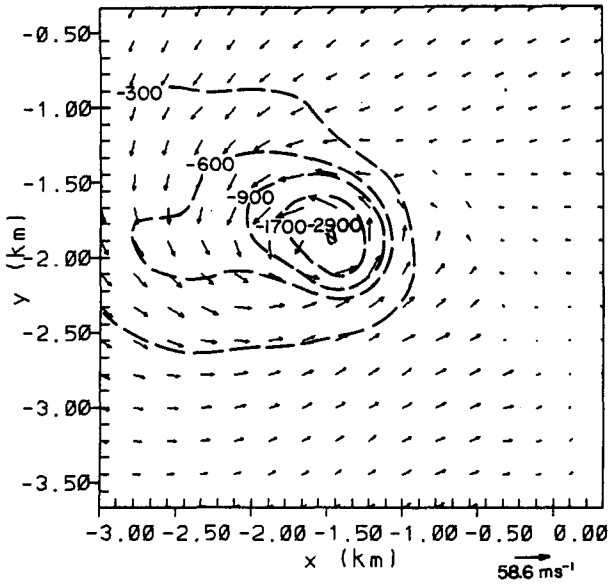

FIG. 21. Same as Fig. 20 except the perturbation pressure loss, in pascals, is shown with the horizontal winds.

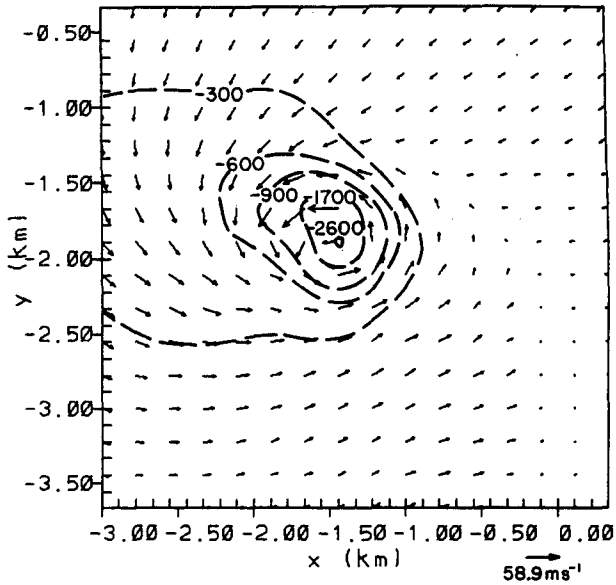

FIG. 23. Same as Fig. 21 except at 215 m.

of the vortex is at 365 m. The updraft maximum of 60 m s^{-1} (Fig. 18), and the perturbation pressure deficit of 30 mb (Fig. 19) is accompanied by tangential winds of 54 m s^{-1}. Figures 20, 22, 24, and 26 show the vertical motion superimposed on the storm-relative horizontal wind vectors at 283, 215, 158, and 11 m, respectively. The corresponding maximum vertical speeds are 56, 51, 45, and 8 m s^{-1}. Figures 21, 23, 25, and 27 depict the perturbation pressure and the storm-relative horizontal winds at 283, 215, 158, and 11 m. The largest pressure deficits are −2900, −2600, −2100, and −1260 Pa, respectively. The maximum horizontal storm-relative winds are 59 m s^{-1} from 283 to 158 m and 51 m s^{-1} at 11 m. Note that the horizontal wind field at 11 m is basically radially inward. This is a result of the frictional lower boundary.

One cannot overlook the vertical continuity of these fields; it is for this reason and the truly impressive magnitudes of each field that the only feature consistent with the above data is, in fact, a tornado.

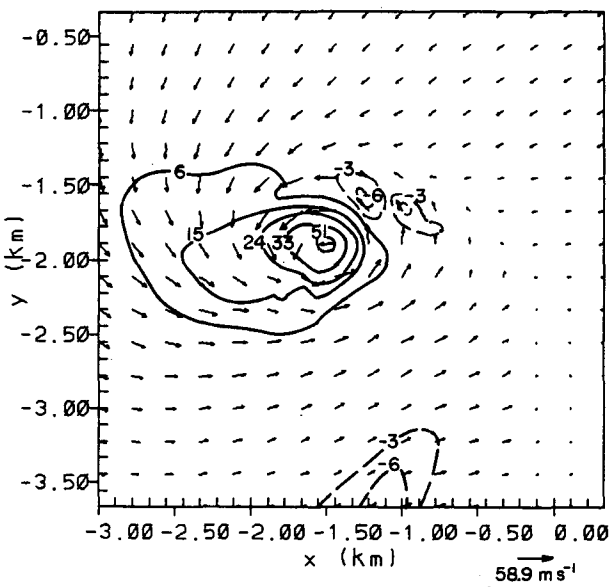

FIG. 22. Same as Fig. 20 except at 215 m.

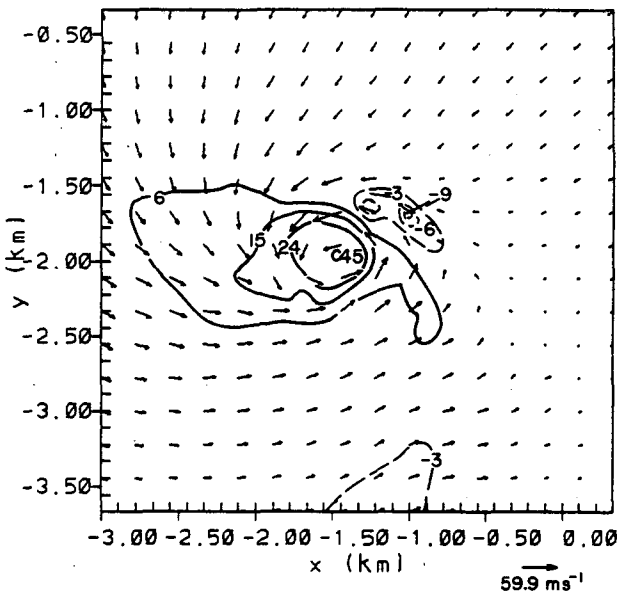

FIG. 24. Same as Fig. 20 except at 158 m.

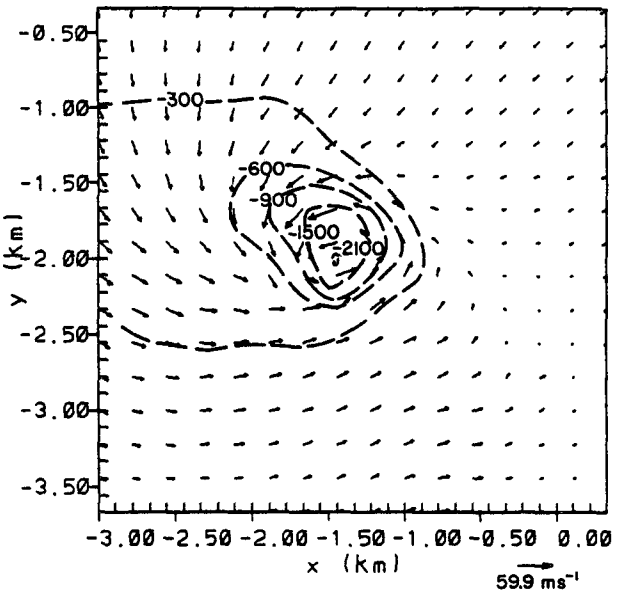

FIG. 25. Same as Fig. 21 except at 158 m.

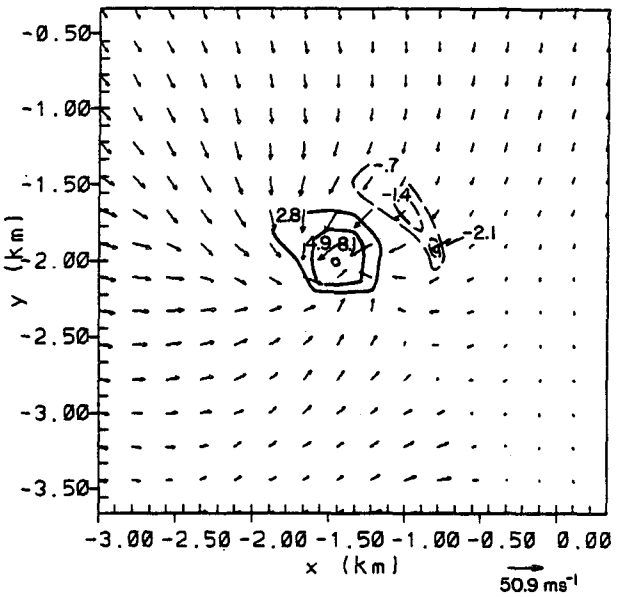

FIG. 26. Same as Fig. 20 except at 11 m.

5. Summary and conclusions

A rotating supercell thunderstorm, or mesocyclone, was simulated using the two-way interactive, nested-grid capability of RAMS. The results exhibited many features in common with observed tornado-producing supercell storms. After 90 min of simulation, two fine grids were initiated, enabling the incipient vortex to be resolved. When the finer grids were spawned, a low pressure tube formed on the east-southeast edge of the storm at the low levels of the storm.[1] The vortex and its associated pressure-deficit tube subsequently built downward into the subcloud layer, where it continually fed upon low-level positive vertical vorticity possibly generated within the downdraft, resulting in further lowering of pressure. This allowed the continued descent of the pressure-deficit tube to the surface. Surface drag forced the surface inflow to converge radially inward to a region where it was forced into a vertical jet. The vortex exhibited maximum updraft strengths of over 60 m s^{-1} as low as 365 m off the ground, pressure deficits as large as 3000 Pa, and tangential wind speeds in excess of 50 m s^{-1}.

A unique feature of this simulation compared to earlier investigations (Smith and Leslie 1978, 1979; Benton and Shapiro 1986) is that the vortex does not build downward from the center of the updraft. Instead, the vortex is initiated at the edge of the updraft in the region of strong horizontal gradient of upward motion. Furthermore, the descending vortex and associated pressure-deficit tube do not simply continue descent to the surface creating a tornado. A more complicated scenario is envisioned in which preexisting surface vorticity possibly associated with the storm-scale downdraft is drawn into the vortex, thereby enriching its vorticity to values large enough to alter the pressure field and

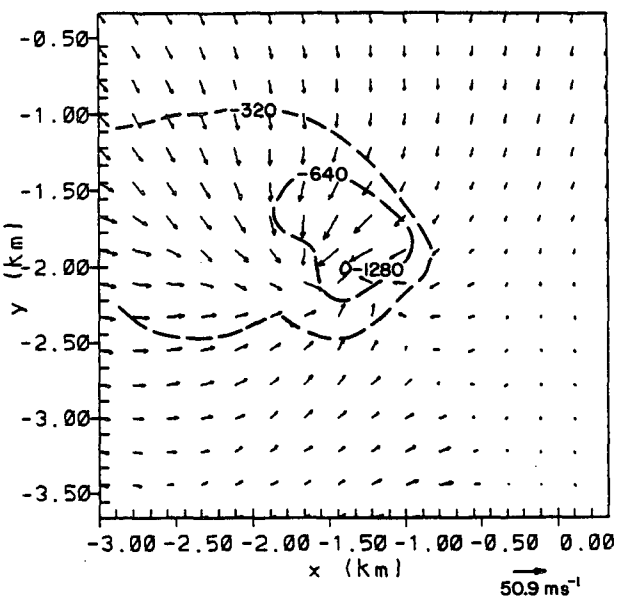

FIG. 27. Same as Fig. 21 except at 11 m.

[1] As a short note, a vortex that forms higher up in the storm could show up as a tornado vortex signature on a Doppler radar. In our case, the genesis of vortex formation was in the lower levels of the updraft; the vortex itself did not become obvious until one looked at horizontal cross sections of the storm-relative winds at lower levels.

allowing the pressure-deficit tube to descend to the surface and form a tornado.

A question that must be addressed is the source of the low-level positive vertical vorticity. Many weightless tracer particles were released at different levels to see their trajectories. We found that air parcels that originated near cloud base and to the north-northeast just outside of the storm moved cyclonically around the northern side of the storm. These parcels then entered the precipitation downdraft. While descending, the parcel's trajectories remained cyclonically curved along the west side. Nearing the surface the parcels moved to the vortex and were ingested by it. Based on this we propose the vertical vorticity is formed along those parcel trajectories that exist through the downdraft. A more complete investigation of this is planned for the future.

It should be recognized that this mechanism is based on a single simulation (or realization) of a supercell thunderstorm performed with an interactive nested grid model in which the fine grids were spawned after 90 min of simulated time. A legitimate question is, Did the vortex form as a result of dynamic adjustments of the wind to the new grid or to the dynamics of the flow field? This question can be answered only by repeating the simulation with the fine grid resolution over the entire domain and for the 105-min period of simulation—an experiment requiring enormous computer resources! On numerous occasions, however, while simulating other storm systems we have spawned fine grids and have been disappointed by the absence of any finescale features. Thus, we do not think this vortex formed in response to the new grid. Nonetheless, we do not claim that the mechanism of excitation of the vortex simulated in this study is the only one responsible for tornado formation.

Wicker and Wilhelmson (1993) also did a simulation of tornadogenesis with a different model. Unlike ours, they spawned a fine grid some 20 min before the tornado formed. The process of tornadogenesis in their run appears to be very similar to ours. Regardless of the actual mechanism responsible for the excitation of the elevated vortex, the minimum of the pressure field located in the horizontal gradient of the updraft, the subsequent downward propagation of the vortex, or pressure tube, to the surface; our simulation provides useful insight into the manner in which tornadogenesis may occur.

Acknowledgments. Thanks are extended to Dr. Robert Walko for his guidance in this subject area, Brenda Thompson for her assistance in preparing this paper, and finally Judy Sorbie-Dunn and Lucy McCall for their aid with the figures.

This research was supported by the National Oceanic and Atmospheric Administration under Contract NA85RAH05045 and the National Science Foundation under Grant ATM-8814913.

Computations were performed on the CSU Atmospheric Science Stardent computer, which was purchased under support of the Army Research Office under Contract DAAL03-86-K-0175.

REFERENCES

Arakawa, A., and V. Lamb, 1981: A potential enstrophy and energy conserving scheme for the shallow water equations. *Mon. Wea. Rev.*, **109,** 18–36.

Benton, G. S., and A. M. Shapiro, 1986: A possible explanation for the sudden spin-up of tornadoes and other small scale atmospheric vortices. Preprints, *16th Conf. on Severe Local Storms,* Boston, MA, Amer. Meteor. Soc., J93–J98.

Brandes, E., 1978: Mesocyclone evolution and tornadogenesis. Some observations. *Mon. Wea. Rev.*, **106,** 995–1011.

——, 1984: Relationships between radar-derived thermodynamic variables and tornadogenesis. *Mon. Wea. Rev.*, **112,** 1033–1052.

Church, C. R., J. T. Snow, G. L. Baker, and E. M. Agee, 1979: Characteristics of tornado-like vortices as function of swirl ratio: A laboratory investigation. *J. Atmos. Sci.*, **36,** 1755–1766.

Clark, T. L., and R. D. Farley, 1984: Severe downslope windstorm calculations in two and three spatial dimensions using anelastic interactive grid nesting: A possible mechanism for gustiness. *J. Atmos. Sci.*, **41,** 329–350.

Cotton, W. R., R. L. George, and K. R. Knupp, 1982: An intense, quasi-steady thunderstorm over mountainous terrain. Part I: Evolution of the storm-initiating mesoscale circulation. *J. Atmos. Sci.*, **39,** 328–342.

——, G. J. Tripoli, R. M. Rauber, and E. A. Mulvihill, 1986: Numerical simulation of the effects of varying ice crystal nucleation rates and aggregation processes on orographic snowfall. *J. Climate Appl. Meteor.*, **25,** 1658–1680.

Cram, J. M., R. A. Pielke, and W. R. Cotton, 1992a: Numerical simulation and analysis of a prefrontal squall line. Part I: Observations and basic simulation results. *J. Atmos. Sci.*, **49,** 189–208.

——, ——, and ——, 1992b: Numerical simulation and analysis of a prefrontal squall line. Part II: Propagation of the squall line as an internal gravity wave. *J. Atmos. Sci.*, **49,** 209–225.

Davies-Jones, R. P., 1984: Streamwise vorticity: The origin of updraft rotation in supercell storms. *J. Atmos. Sci.*, **41,** 2291–3006.

Flatau, P. J., G. J. Tripoli, J. Verlinde, and W. R. Cotton, 1989: The CSU RAMS cloud microphysics module: General theory and code documentation. Atmospheric Science Paper No. 451, 88 pp. [Available from the Dept. of Atmospheric Science, Colorado State University, Fort Collins, CO 80523.]

Grasso, Lewis D., 1992: A numerical simulation of tornadogenesis. Atmospheric Science Paper No. 495, 102 pp. [Available from the Dept. of Atmospheric Science, Colorado State University, Fort Collins, CO 80523.]

Klemp, J. B., and R. B. Wilhelmson, 1978a: The simulation of three-dimensional convective storm dynamics. *J. Atmos. Sci.*, **35,** 1070–1096.

——, and ——, 1978b: Simulations of right- and left-moving storms produced through storm splitting. *J. Atmos. Sci.*, **35,** 1097–1110.

——, and R. Rotunno, 1983: A study of the tornadic region within a supercell thunderstorm. *J. Atmos. Sci.*, **40,** 359–377.

——, R. B. Wilhelmson, and P. Ray, 1981: Observed and numerically simulated structure of a mature supercell thunderstorm. *J. Atmos. Sci.*, **38,** 1558–1580.

Lemon, R. L., and C. A. Doswell III, 1979: Severe thunderstorm evolution and mesocyclone structure as related to tornadogenesis. *Mon. Wea. Rev.*, **107,** 1184–1197.

Lewellen, S. W., 1976: Theoretical models of the tornado vortex. *Proc. Symp. on Tornadoes: Assessment of Knowledge and Implications for Man,* Lubbock, TX, Texas Tech University, 107–143.

Lilly, D. K., 1962: On the numerical simulation of buoyant convection. *Tellus*, **14**, 148–172.

——, 1986a: The structure, energetics, and propagation of rotating convective storms. Part I: Energy exchange with the mean flow. *J. Atmos. Sci.*, **43**, 113–125.

——, 1986b: The structure, energetics, and propagation of rotating convective storms. Part II: Helicity and storm stabilization. *J. Atmos. Sci.*, **43**, 126–140.

Louis, J. F., 1979: A parametric model of vertical eddy fluxes in the atmosphere. *Bound.-Layer Meteor.*, **17**, 187–202.

Ray, P. S., Ed., 1986: *Mesoscale Meteorology and Forecasting*. Amer. Meteor. Soc., 793 pp.

——, C. E. Hane, R. P. Davies-Jones, and R. L. Alberty, 1976: Tornado–parent storm relationship deduced from a dual-Doppler radar analysis. *Geophys. Res. Lett.*, **3**, 721–723.

——, B. C. Johnson, K. W. Johnson, J. S. Bradberry, J. J. Stephens, K. K. Wagner, R. B. Wilhelmson, and J. B. Klemp, 1981: The morphology of several tornadic storms on 20 May 1977. *J. Atmos. Sci.*, **38**, 1643–1663.

Rotunno, R., and J. B. Klemp, 1985: On the rotation and propagation of simulated supercell thunderstorms. *J. Atmos. Sci.*, **42**, 271–292.

Schlesinger, R. E., 1978: A three-dimensional numerical model of an isolated thunderstorm. Part I: Comparative experiments for variable ambient wind shear. *J. Atmos. Sci.*, **35**, 690–713.

——, 1980: A three-dimensional numerical model of an isolated thunderstorm. Part II: Dynamics of updraft splitting and mesovortex couplet evolution. *J. Atmos. Sci.*, **37**, 395–420.

Schmidt, J. M., and W. R. Cotton, 1990: Interactions between upper and lower tropospheric gravity waves on squall line structure and maintenance. *J. Atmos. Sci.*, **47**, 1205–1222.

Smagorinsky, J., 1963: General circulation experiments with the primitive equations. Part I: The basic experiment. *Mon. Wea. Rev.*, **91**, 99–164.

Smith, R. K., and L. M. Leslie, 1978: Tornadogenesis. *Quart. J. Roy. Meteor. Soc.*, **104**, 189–199.

——, and ——, 1979: A numerical study of tornadogenesis in a rotating thunderstorm. *Quart. J. Roy. Meteor. Soc.*, **105**, 107–127.

Snow, J. T., 1982: A review of recent advances in tornado vortex dynamics. *Rev. Geophys. Space Phys.*, **20**, 953–964.

Tripoli, G. J., and W. R. Cotton, 1980: A numerical investigation of several factors contributing to the observed variable intensity of deep convection over South Florida. *J. Appl. Meteor.*, **19**, 1037–1063.

——, and ——, 1982: The Colorado State University three-dimensional cloud/mesoscale model—1982. Part I: General theoretical framework and sensitivity experiments. *J. Rech. Atmos.*, **16**, 185–220.

——, and ——, 1986: An intense quasi-steady thunderstorm over mountainous terrain. Part IV: Three-dimensional numerical simulation. *J. Atmos. Sci.*, **43**, 894–912.

——, and ——, 1989a: A numerical study of an observed orogenic mesoscale convective system. Part 1. Simulated genesis and comparison with observations. *Mon. Wea. Rev.*, **117**, 273–304.

——, and ——, 1989b: A numerical study of an observed orogenic mesoscale convective system. Part 2. Analysis of governing dynamics. *Mon. Wea. Rev.*, **117**, 305–328.

Walko, R. L., 1988: The plausibility of substantial dry-adiabatic subsidence in a tornado core. *J. Atmos. Sci.*, **45**, 2251–2267.

Ward, N. B., 1972: The exploration of certain features of tornado dynamics using a laboratory model. *J. Atmos. Sci.*, **29**, 1194–1204.

Weisman, M., and J. Klemp, 1982: The dependence of numerically simulated convective storms on vertical wind shear and buoyancy. *Mon. Wea. Rev.*, **110**, 504–520.

——, and ——, 1984: The structure and classification of numerically simulated convective storms in directionally varying wind shears. *Mon. Wea. Rev.*, **112**, 2479–2498.

Wicker, L. J., and R. B. Wilhelmson, 1993: Numerical simulation of tornadogenesis within a supercell thunderstorm. *The Tornado: Its Structure, Dynamics, Prediction and Hazards, Geophys. Monogr.*, No. 79, Amer. Geophys. Union, 75–88.

Wilhelmson, R. B., and J. Klemp, 1981: A three-dimensional numerical simulation of splitting severe storms on 3 April 1964. *J. Atmos. Sci.*, **38**, 1581–1600.